# Dual-Phase $CsPbBr_3$–$CsPb_2Br_5$ Perovskite Thin Films via Vapor Deposition for High-Performance Rigid and Flexible Photodetectors

*Guoqing Tong, Huan Li, Danting Li, Zhifeng Zhu, Enze Xu, Guopeng Li, Linwei Yu,* Jun Xu, and Yang Jiang**

**Inorganic perovskites with special semiconducting properties and structures have attracted great attention and are regarded as next generation candidates for optoelectronic devices. Herein, using a physical vapor deposition process with a controlled excess of $PbBr_2$, dual-phase all-inorganic perovskite composite $CsPbBr_3$–$CsPb_2Br_5$ thin films are prepared as light-harvesting layers and incorporated in a photodetector (PD). The PD has a high responsivity and detectivity of 0.375 A $W^{-1}$ and $10^{11}$ Jones, respectively, and a fast response time (from 10% to 90% of the maximum photocurrent) of ≈280 µs /640 µs. The device also shows an excellent stability in air for more than 65 d without encapsulation. Tetragonal $CsPb_2Br_5$ provides satisfactory passivation to reduce the recombination of the charge carriers, and with its lower free energy, it enhances the stability of the inorganic perovskite devices. Remarkably, the same inorganic perovskite photodetector is also highly flexible and exhibits an exceptional bending performance (>1000 cycles). These results highlight the great potential of dual-phase inorganic perovskite films in the development of optoelectronic devices, especially for flexible device applications.**

## 1. Introduction

Halide perovskites with the formula of $ABX_3$, especially organic–inorganic hybrid perovskites, have emerged as next-generation candidates for their high mobility, wide absorption spectrum, and high power conversion efficiency, and they have been successfully applied in solar cells, photodetectors (PDs), light-emitting diodes (LEDs), and lasers.[1–7] Hybrid organic–inorganic perovskites used for solar cells have recently reached the highest recorded conversion efficiency (PCE) of 22.1%;[8] however, the stability of these solar cells in humid environments remains a challenge for their practical application. Very recently, the all-inorganic perovskite material $CsPbBr_3$ has been introduced as a candidate for substitution in the solar cells and presented a high PCE of 6.7% and impressive stability under high humidity conditions (RH ≈ 90–95%) for more than three months.[9] Therefore, the pure inorganic perovskites provide a promising material for fabricating optoelectronic devices such as solar cells, light-emitting diodes, and photodetectors for their enhanced resistance against degradation from humidity and improved thermal stability.[10–13] For example, highly phase-stable $\alpha$-$CsPbI_3$ perovskite quantum dots (QDs) with an open-circuit voltage of 1.23 V and an efficiency of 10.77% were fabricated and function as light-emitting diodes with a low turn-on voltage and tunable emission wavelength.[14] Zeng and co-workers reported a pure inorganic perovskite photodetector, showing a fast response on flexible substrates under ≈445 nm illumination and a high stability after bending for more than 1000 cycles.[15,16] A fast and reproducible way to fabricate all-inorganic cesium lead halide perovskite nanocrystals was also demonstrated in organic solvent for the first time, exhibiting a good on/off photocurrent ratio of $10^5$.[17]

In the past years, many techniques for hybrid organic perovskites, including the classic one-step spin-coating method, the two-step solution method and vapor deposition methods, have been investigated to obtain a high-quality perovskite film.[18] However, a fast reaction process and organic solvent in the solution have negatively influenced the morphology and crystallization of the hybrid perovskite films.[19] The vapor deposition methods, including co-vapor deposition, vapor-assisted solution processing, all-vacuum deposition, etc., have also been proposed to prepare hybrid organic perovskite films, providing a great advantage toward obtaining uniform, full-coverage, and highly crystalline materials using mature industrial processes that can be used for large-scale manufacturing.[19–21] In addition, nonsolvent deposition procedures can effectively avoid damage

Dr. G. Tong, H. Li, D. Li, Dr. Z. Zhu, E. Xu, Dr. G. Li, Prof. Y. Jiang
School of Materials Science and Engineering
Hefei University of Technology
Hefei 230009, P. R. China
E-mail: apjiang@hfut.edu.cn

Dr. G. Tong, Prof. L. Yu, Prof. J. Xu
National Laboratory of Solid State Microstructures and School of Electronics Science and Engineering/Collaborative Innovation Centre of Advanced Microstructures
Nanjing University
Nanjing 210093, P. R. China
E-mail: yulinwei@nju.edu.cn

The ORCID identification number(s) for the author(s) of this article can be found under https://doi.org/10.1002/smll.201702523.

DOI: 10.1002/smll.201702523

to the film and can reduce the metastable state in the perovskite film, to enhance the stability.[19,22,23] Similar to hybrid perovskite films, inorganic perovskites formed by solution-processing and vapor deposition approaches have been widely investigated in solar cells, light-emitting devices and photodetectors.[17,24–27] Since CsBr is sensitive to humidity, vapor deposition provides a vacuum environment to ensure no solvent residue existing in the film during the reaction, and the vapor method is also suitable for the deposition of insoluble materials.[25] For example, pure $CsPbI_3$, $CsPbIBr_2$, and $CsPbI_2Br$ films were prepared by vacuum deposition as light-harvesting layers in solar cells and exhibited a high photovoltaic performance.[24,25,28]

Herein, we report for the first time a dual-phase inorganic perovskite ($CsPbBr_3$–$CsPb_2Br_5$) as a light-harvesting layer by a physical vapor deposition method on the rigid and flexible substrates. The CsBr and $PbBr_2$ films are sequentially deposited via thermal evaporation on the substrates with a controllable excess of $PbBr_2$ through the regulation of the thickness, and then, a postannealing step is performed in air at 130 °C to enable the formation of the dual-phase inorganic perovskite. The halogen ions ($Br^-$) were found to be enriched on the surface of the inorganic perovskite films, resulting in the presence of a wide bandgap semiconductor $CsPb_2Br_5$ in the film and consequently a self-passivation phenomenon on the interface, which could have a positive effect in reducing charge recombination. In addition, a high responsivity of 0.375 A $W^{-1}$ and detectivity of $2.96 \times 10^{11}$ Jones were obtained with the structure of Au/dual-phase inorganic perovskite/Au, and it presented a fast response of 280 µs/640 µs under 800 Hz and a high stability in air for more than 65 d. Impressively, a flexible inorganic perovskite PD was also realized with a responsivity and detectivity of 25 mA $W^{-1}$ and $2.2 \times 10^{11}$ Jones, respectively, via the same process, and extra stability with a fluctuation of less than 20% was achieved after bending 1000 times. These results demonstrate that the dual-phase inorganic perovskite film via the vapor deposition method is a potential candidate in optoelectronic devices, especially in flexible devices.

## 2. Results and Discussion

The CsBr and $PbBr_2$ film were deposited on the substrates sequentially by controlling the thickness of films in the vacuum system, maintaining a controllable excess of $PbBr_2$, and annealing in air for several minutes, as depicted in the experimental section. The characterization of the dual-phase all inorganic perovskite films by the vapor phase method is presented in **Figure 1**. Figure 1c shows the crystallization structure of $CsPbBr_3$ and $CsPb_2Br_5$. The $CsPbBr_3$ exhibits a cubic (Pm3m) phase, where a 3D framework of corner-connected $PbBr_6$ octahedra with $Cs^+$ cations is located between the octahedra, as presented in Figure 1c.[29] In contrast, tetragonal $CsPb_2Br_5$ is detected in the presence of excess $PbBr_2$, and the Cs ions are sandwiched between two layers of Pb–Br-coordinated polyhedrons with an indirect bandgap of ≈2.9 eV. The formation of $CsPb_2Br_5$ can be explained by the following mechanism[29–31]

$$CsBr + PbBr_2 \rightarrow CsPbBr_3 \tag{1}$$

$$CsPbBr_3 + PbBr_2 \rightarrow CsPb_2Br_5 \tag{2}$$

Figure 1d,f shows the selected area electron diffraction (SAED) patterns of the inorganic perovskite film after annealing, where the diffraction spots, associated with the (110) and (−110) crystal planes, can be indexed to the [001] zone axis of tetragonal $CsPb_2Br_5$. It is consistent with the simulation from Figure 1f, which suggests that the $CsPb_2Br_5$ presented at the interface of the $CsPbBr_3$. To further investigate the present $CsPb_2Br_5$ phase in the inorganic perovskite film, the X-ray photoelectron spectroscopy (XPS) measurement was conducted (Figure S1, Supporting Information). No significant shift was observed for the Pb 4f and Br 3d peaks in the XPS spectra due to the same element valence band from $CsPbBr_3$ and $CsPb_2Br_5$.[31] The atom ratio of Cs to Pb and Br from XPS, as listed in Table S1 (Supporting Information), is consistent with our conjecture.

$CsPbBr_3$ was formed with the ratio of the CsBr/$PbBr_2$ near 1:1, and the $CsPb_2Br_5$ formed with a ratio up to 1:2 in the solution process. However, in our work, the $CsPbBr_3$ film deposited from the vapor deposition method contains the 150 nm CsBr film and 210 nm $PbBr_2$ film. In addition, the dual-phase inorganic perovskite film was prepared by the same method with the thickness of CsBr and $PbBr_2$ near 90 and 210 nm, respectively. A photograph of the dual-phase inorganic perovskite film on the glass substrate with the size of 2.5 × 1.5 cm, presented in Figure 1a (inset), is quite uniform, and the film shows a green color under UV light illumination. The absorption spectrum of the inorganic perovskite is shorter than ≈535 nm, which shifts to lower wavelength by ≈10 nm compared to previous reports of the pure $CsPbBr_3$ film.[9] The PL emission spectra of $CsPbBr_3$ and dual-phase $CsPbBr_3$–$CsPb_2Br_5$ (Figure S2, Supporting Information) are 534 and 530 nm, respectively. The blue spectral shift can be ascribed to the $CsPb_2Br_5$ phase appearing in the film, leading to an enhanced band gap of the inorganic perovskite film. According to the UV–vis absorption spectrum in Figure 1a, we can infer that the inorganic perovskite has a favorable absorption capability and a direct bandgap. Since the blueshift of the film has significant influence on the bandgap energy ($E_g$) of the film, we calculate the $E_g$ of the inorganic perovskite by the Kubellka–Munk equation, as shown in Figure S3 (Supporting Information). The $E_g$ of ≈2.39 eV is obtained based on a plot of $(\alpha h\nu)^2$ versus the photon energy ($h\nu$).

After photolithography and lift-off, the Ti/Au electrodes with 2 µm spacing and 200 µm lengths were defined on the $P^+$-Si substrates (Figure S4, Supporting Information). The CsBr and $PbBr_2$ films were sequentially deposited on the substrates via the vapor method, as shown in Figure S5 (Supporting Information). Since the dual-phase perovskite in this work provided a wide bandgap of 2.39 eV, a 365 nm incident light was illuminated on the device with the power intensity of 1.7 mW $cm^{-2}$. From **Figure 2**b, we can clearly observe that the $I$–$V$ curve for the device presents a linear relationship, suggesting that the ohmic-contact was formed between the perovskite film and the electrons. The current under dark and light illumination under a bias voltage of −5 V for the inorganic perovskite PD is $-2 \times 10^{-10}$ A and $-2.75 \times 10^{-9}$ A, respectively. As an important characteristic for the photodetector, the responsivity ($R$) is defined as the photocurrent generated per unit power of the

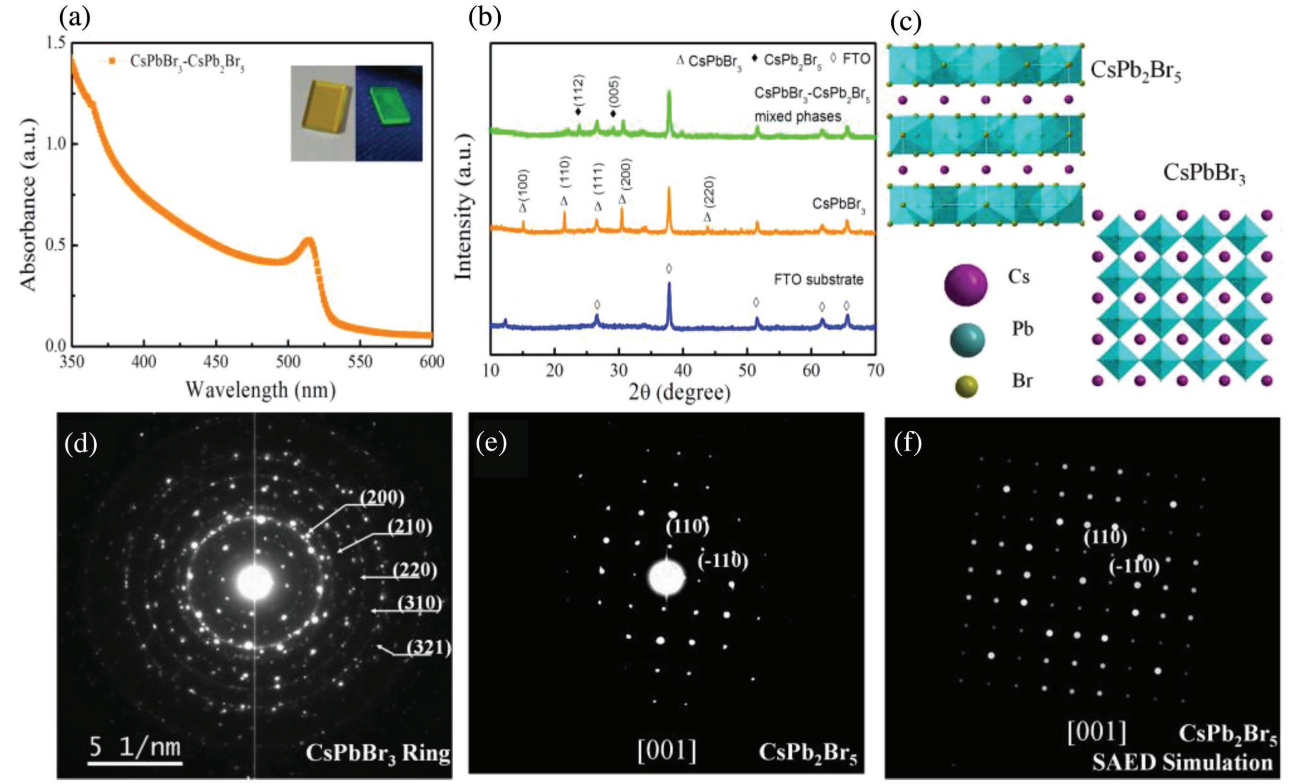

**Figure 1.** a) UV–vis absorbance spectrum of the inorganic perovskite film; insets: a photograph of the inorganic perovskite film on a glass substrate and the same under UV light illumination with a size of 2.5 × 1.5 cm. b) The XRD patterns of the inorganic perovskite film. c) Crystal structures of the inorganic perovskite $CsPbBr_3$ and $CsPb_2Br_5$. d) SAED pattern of $CsPbBr_3$. e) SAED pattern and f) SAED simulation pattern of $CsPb_2Br_5$.

incident light on the effective activity, which can be expressed as follows

$$\mathrm{R}(\mathrm{A}\cdot\mathrm{W}^{-1}) = (I_{\mathrm{light}} - I_{\mathrm{dark}})/\mathrm{PA} \tag{3}$$

where $I_{\mathrm{light}}$ and $I_{\mathrm{dark}}$ are the current under light illumination and dark conditions, respectively, $P$ is the powder intensity of the incident light, and $A$ is the active area in our device. Based on the above equation, the extracted responsivity is 0.375 A $W^{-1}$ for the device under 365 nm illumination with a bias of −5 V, which is higher than the values in previous reports based on the hybrid perovskite PDs and commercial Si photodetectors (<0.2 A $W^{-1}$).[15,32] The corresponding detectivity ($D^*$) of the device can be calculated to be $2.96 \times 10^{11}$ Jones (Jones = cm $Hz^{1/2}$ $W^{-1}$) by the following equation[33]

$$D^* = \frac{R\sqrt{A}}{\sqrt{2qI_{\mathrm{d}}}} \tag{4}$$

where $q$ is the elementary charge. To further investigate the light response of the detector in the region ranging from 365 to 535 nm, we obtained the $I$–$V$ curves by varying the laser illumination intensity at different wavelength (365, 405, and 535 nm, presented in Figure S6, Supporting Information). The photocurrent increased with the enhancement of the incident power intensity. More important, the photocurrent exhibited a strong dependence on the light intensity with a best fitting of

$$I_{\mathrm{p}} = aP^{b} \tag{5}$$

where $I_{\mathrm{p}}$, $a$ and $b$ stand for the photocurrent, proportionality constant, and light power intensity, respectively. The fitting values were 3.19, 3.14 and 1.44, and the $b$ values were 0.88, 0.81, and 0.91 for the wavelength of 365, 405, and 532 nm, respectively.

In addition, the response characteristics of the detector were also determined by the time-dependent photocurrent under a periodic off/on illumination (365 nm) at a bias of −1 and −5 V, respectively. As depicted in Figure 2d, the current increased with the light irradiation on, which delivers a stable and repeatable current. What's more, the ON/OFF ratios of the devices are 4 and 380 for bias of −1 and −5 V, respectively.

Apart from the response wavelength and the detectivity and responsivity of the devices, the response time is another crucial parameter of the photodevices, which is defined as the photocurrent increase from 10% to 90% of the highest value.[34–36] As depicted in **Figure 3**a, the device is tested under 365 nm incident light with a mechanical chopper, exhibiting an excellent stability and reproducibility. More importantly, the rise and fall times ($t_{\mathrm{rise}}/t_{\mathrm{fall}}$) are 280 and 640 µs, which are obviously faster than those of previous hybrid or inorganic nanosheets, nanocrystals and films, as listed in **Table 1**. A cutoff frequency ($f_{3\mathrm{dB}}$) of 3 dB can also be extracted by the following equation:[37] $f_{3\mathrm{dB}} = 0.35/t_{\mathrm{rise}}$, and the 3 dB cutoff of the device is estimated to be 1.25 KHz. In addition, the differential signal of

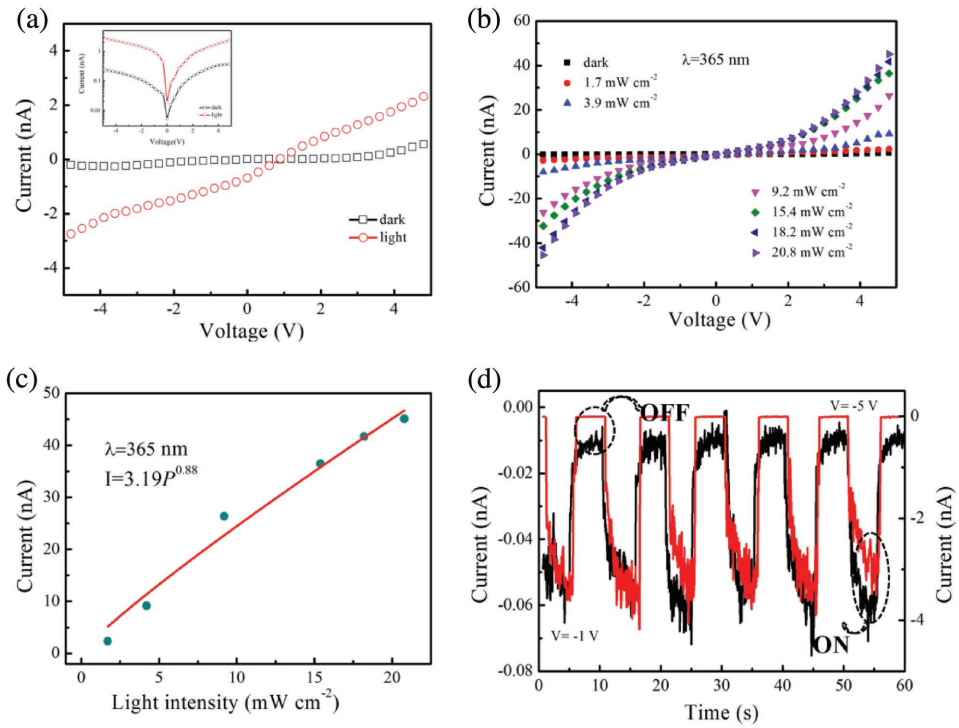

**Figure 2.** a) The *I*–*V* curve of the inorganic perovskite device in the dark and the one under illumination with 365 nm light (1.7 mW cm$^{-2}$), insets: corresponding logarithmic *I*–*V* curve. b) The inorganic perovskite device under 365 nm irradiation with varying intensity from 1.7 to 20.8 mW cm$^{-2}$. c) Photocurrent density measured as a function of incident light intensity at a bias voltage of –5 V. d) Photoresponse of inorganic perovskite device under –1 and –5 V.

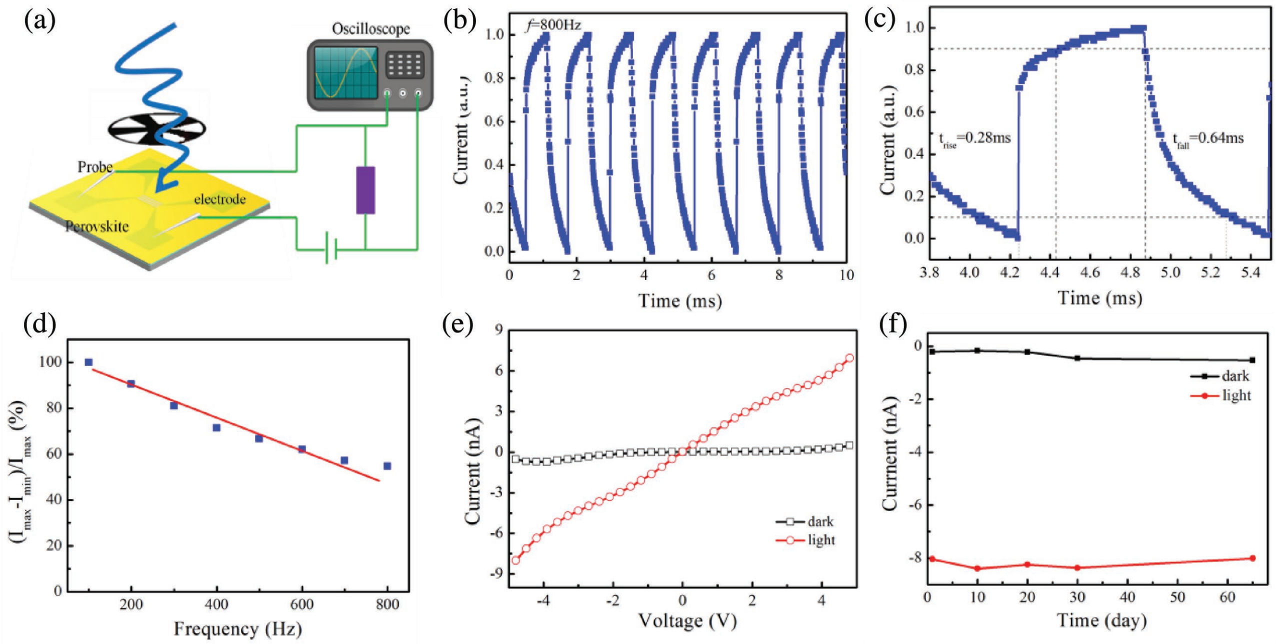

**Figure 3.** a) Schematic illustration of the inorganic perovskite device to measure the photoresponse speed. b) Inorganic perovskite devices under 365 nm illumination at a frequency of 800 Hz. c) The corresponding magnified and normalized plots of one response cycle. d) Frequency dependence of relative balance value (($I_{\max} - I_{\min}$)/$I_{\max}$). e) *I*–*V* curve of the inorganic perovskite device after storage in air for 65 d. f) The stability of the inorganic perovskite devices stored in the air.

**Table 1.** Performance comparison of the inorganic perovskite PDs from present and previous reports.

| Device | Method | Wavelength [nm] | $R$ [A W$^{-1}$] | $D^*$ [Jones] | Response time | Refs. |
|---|---|---|---|---|---|---|
| $CsPbBr_3$–$CsPb_2Br_5$ film | Vapor | 365 | 0.375 | $2.96 \times 10^{11}$ | 280 µs/640 µs | Our work |
| $CsPbI_3$ NCs | Solution | 405 | – | – | 24 ms/29 ms | [17] |
| Graphene–$CsPbBr_{3-x}I_x$ | Solution | 405 | $8.2 \times 10^{8}$ | $2.4 \times 10^{16}$ | 0.81 s/3.65 s | [38] |
| $\alpha$-$CsPbI_3$– $NaYF_4$:Yb,Er QD | Solution | 525 | 1.5 | – | 5 ms/5 ms | [39] |
| $CsPbBr_3$ nanosheets | Solution | 450 | – | – | 17.8 ms/14.7 ms | [40] |
| $CsPb(Br/I)_3$ nanorods | Solution | 532 | – | – | 0.68 s/0.66 s | [41] |
| $CsPbBr_3$ nanosheets | Solution | 442 | 0.25 | – | 19 µs/25 µs | [15] |
| $MAPbBr_3$ nanowires | Solution | 420 | – | – | 0.12 s/0.086 s | [42] |
| $MAPbI_3$ film | Solution | 365 | 3.49 | – | 0.2 s/0.2 s | [43] |
| $MAPbI_3$ nanowires/graphene | Solution | 633 | $2.6 \times 10^{6}$ | – | 55 s/75 s | [44] |

the devices is also summarized in Figure 3d as a function of the frequency. Clearly, the the relative balance $(I_{\max} - I_{\min})/I_{\max}$ of the devices only decreased by 40% at a high frequency of 600 Hz, indicating that the inorganic perovskite devices can work at even a high frequency.

The stability of the perovskite devices has been regarded as an important issue; however, in most cases, the unstable hybrid perovskite materials decomposed easily and reformed lead (II) iodide, leading to a decrease in the performance and limiting its practical application. Surprisingly, in our work, the inorganic perovskite devices fabricated via the vapor deposition method provided a high stability in air with a humidity above 50% without encapsulation. As seen in Figure 3e,f, the $I$–$V$ curve of the devices (inset) showing ohmic-contact suggests that there was no obvious decomposition in the perovskite film and provided good contact between the film and electrodes after being stored in the air over a month and over 65 d. Furthermore, the lack of significant decrease (under 365 nm illumination with the powder intensity of ≈3.9 mW cm$^{-2}$) indicates that the inorganic perovskite shows a superior stability.

The high performance and stability of the inorganic perovskite PD in our work can be explained by the dual phases in the absorption layer. It is important to note that the ohmic contact between the film and electrode can effectively decrease the contact barrier, providing a faster transportation path, which significantly increases the photocurrent and the responsivity.[45] The excitons are generated in the inorganic perovskite film with light irradiation on the device, and both of them are swept outside the perovskite thin film and injected into the electrodes under the built-in field.[46–48] However, the recombination of the charge carrier at the interface and the nonradiation recombination compete with the extraction of the photogenerated charges, as seen in **Figure 4**a,b.[49] According to the previous work, $CsPbBr_3$ and $CsPb_2Br_5$ (Figure 4c) show a wide bandgap of 2.33 and 2.9 eV, respectively. Compared to $CsPbBr_3$, $CsPb_2Br_5$ contains an abundance of halogens, which accumulate at the interface and connect with the cations to prevent the trapping of the excited electrons by surface defects and reduce the charge carrier recombination (seen in Figure 4d). To further investigate the passivation effect, the $I$–$V$ curve was conducted under 532 nm illumination for the pure CsPbBr3 and the dual phases perovskite film. As seen in Figure S7 (Supporting Information), the dark and light current of the $CsPbBr_3$ lower than that of the $CsPbBr_3$–$CsPb_2Br_5$. The defects at the $CsPbBr_3$ interface as the recombination centers will to some extent increase electron recombination, thus simultaneously enhancing the dark current and decreasing the light current. This self-passivation phenomenon is similar to the $PbX_2$ passivation in the hybrid perovskite and traditional QDs with halogen ions.[10,50] A second effect of $CsPb_2Br_5$ is a decrease of the free energy of the inorganic perovskite.[30] Compared to $CsPbBr_3$, $CsPb_2Br_5$ formed at the interface with a lower free energy prevents the decomposition of perovskite, improving the stability of the devices.

Because the inorganic perovskite ($CsPbX_3$) materials can be deposited by vapor deposition at a lower temperature without an extra-high annealing temperature, the inorganic perovskite can be prepared upon the flexible substrates. In comparison to previous flexible PDs with the solution method, the vapor deposition process provides the possibility of higher coverage and a larger scale device. **Figure 5**c is the structure of the flexible inorganic PDs. Under illumination (365 nm), the $I$–$V$ curve is quasilinear and symmetric, and the photocurrent increased with increasing light intensity from 0.2 to 5.5 mW cm$^{-2}$. These results indicate that an ohmic-like contact with the Si

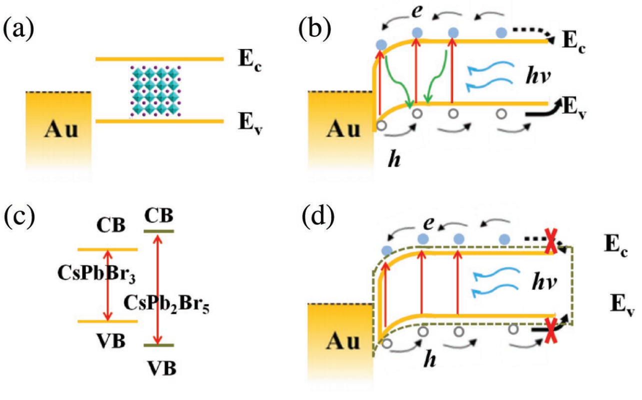

**Figure 4.** The energy band diagram of the device under a) equilibrium condition and b) illumination. c) Bandgap of the $CsPbBr_3$ and $CsPb_2Br_5$. d) Energy band diagram of the device under illumination with $CsPb_2Br_5$ passivation.

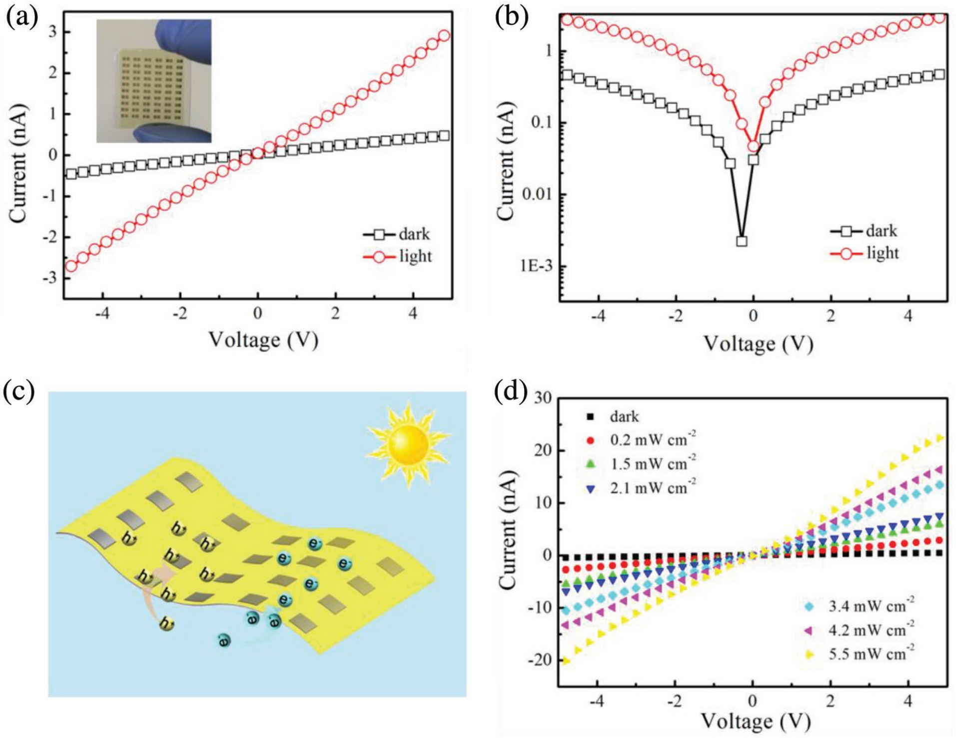

**Figure 5.** a) The *I*–*V* curve of the inorganic perovskite device in the dark and under illumination with 365 nm light (0.2 mW cm$^{-2}$); inset: photograph of the flexible inorganic perovskite device. b) Corresponding logarithmic *I*–*V* curve. c) The structure illustration of the flexible inorganic perovskite device. d) The *I*–*V* curve of a flexible inorganic perovskite device under 365 nm irradiation with varying intensities.

substrates is formed, showing a remarkable dependence on the wavelength of the incident light. Figure 5a,b is the dark and light photocurrent under a bias voltage of −5 V for the flexible perovskite PDs. The current under dark and light illumination is $-4.6 \times 10^{-10}$ A and $-2.71 \times 10^{-9}$ A, respectively. In addition, the corresponding *R* and *D** are calculated to be 25 mA W$^{-1}$ and $2.2 \times 10^{11}$ Jones, respectively.

The stability of the flexible inorganic perovskite PDs has also been investigated in the above experiment. To realize the application, the performance stability and especially the electronic properties of the flexible PD were determined under mechanical bending. In addition, the electronic performance of the devices under various bending curvatures. As shown in the inset pictures in **Figure 6**a, the five different bending states (I, II, III, IV, and V) are depicted, and the photocurrents and dark currents of the flexible devices exhibited no change at a fixed voltage of 5 V for the various bending states, indicating that the flexible devices maintain a high performance, and there is no obvious influence from the external bending stress. To further investigate the stability of the flexible devices, we conducted the *I*–*V* curves after bending more than 1000 times. Compared to the pristine device with a photocurrent of −13.26 nA, a high current of −10.03 nA was obtained after bending 1000 times at a bias voltage of −5 V. Only a 24% decrease was detected, which suggests that the device is extremely stable, opening opportunities for fundamental research on inorganic perovskite materials and introducing vapor deposition as a method for the fabrication of optoelectronics.

## 3. Conclusions

In conclusion, we proposed a new inorganic perovskite film via a vapor deposition method using a dual-phase inorganic material ($CsPbBr_3$–$CsPb_2Br_5$ mixed phases) for the first time. A high responsivity and detectivity of 0.375 A W$^{-1}$ and ≈$10^{11}$ Jones with a high stability in air were obtained for this material on silicon substrates. Furthermore, the inorganic perovskite device shows a faster response time of ≈280 µs/640 µs for the rise and fall times, respectively. The passivation of $CsPb_2Br_5$ at the interface can effectively reduce the charge carrier recombination and improve the stability of the inorganic perovskite. Interestingly, the flexible inorganic perovskite device is also realized at a lower deposition temperature and without additional high-temperature heat treatment. Furthermore, the flexible device exhibits excellent flexibility after 1000 bending cycles. This high performance indicates that inorganic dual-phase perovskite films of $CsPbBr_3$–$CsPb_2Br_5$ have great potential in optoelectronics due to their simple, low-temperature, and low-cost fabrication.

## 4. Experimental Section

*Synthesis and Characterization of Inorganic Perovskite Films*: The inorganic perovskite film was formed by vapor deposition. First, the CsBr (99.9%), $PbBr_2$ (99.99%) powder and substrates were placed in the vacuum system and pumped to ≈$10^{-4}$ Pa. Second, the CsBr and $PbBr_2$ thin films were successively deposited on the substrates by

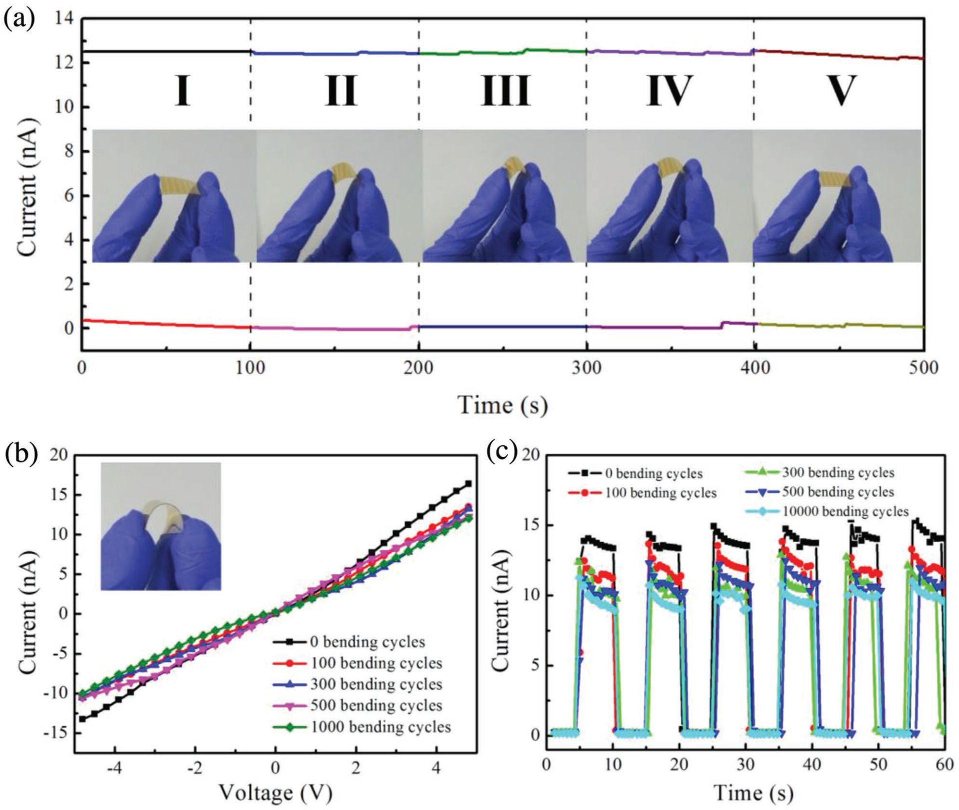

**Figure 6.** *I*–*t* curves of the flexible inorganic perovskite device when bent at different curvatures under a bias voltage of 5 V; inset: corresponding photographs of the device at the different bending states. b) *I*–*V* curve and photoresponse of the flexible inorganic perovskite device after 1000 bending cycles; inset: photograph of the flexible device at the bending state. c) The photoresponse of the flexible device after bending for various numbers of cycles.

thermal evaporation. The thickness of the CsBr (90 nm) and $PbBr_2$ (210 nm) films with the evaporation rate of $\approx$0.4 and $\approx$1 Å s$^{-1}$ was monitored by a quartz crystal microbalance, respectively, to form the dual-phase inorganic perovskite film. Finally, the inorganic perovskite film was annealed at 130 °C for 10 min in air. The phases of the as-synthesized inorganic perovskite were identified by X-ray powder diffraction (XRD) utilizing Cu K$\alpha$ radiation with scanning range of 10° to 70°, and the composition of the inorganic perovskites was analyzed by XPS (Thermo ESCALAB 250). The morphology of the samples was investigated by field emission scanning electron microscopy (Sigma Zeiss). The TEM images were obtained on a JEM-2100 field emission transmission electron microscope. The absorption and PL spectra of the inorganic perovskite films were measured by a UV–vis spectrophotometer (UV-2550) and a Hitachi F-4600 fluorescence spectrophotometer, respectively.

*Device Construction and Measurements*: Both the Si-wafer and flexible substrates were cleaned with acetone (Si wafer only), ethyl alcohol, and deionized water with 20 min of sonication, each, and then dried in Ar. Ti/Au (15/20 nm) electrodes with a 2 µm spacing were defined by photolithography on $SiO_2$ (300 nm)/p+-Si substrates via the electron beam (EB) system following a lift-off process. The flexible substrates were defined by a shadow mask with a spacing of (1 mm × 50 µm) using Au (35 nm) as the electrodes. The inorganic perovskite film was deposited on the substrates by a vapor deposition method as mentioned in the synthesis section. The electrical measurements were conducted by a semiconductor parameter analyzer system (Keithley 4200-SCS). The photoresponse properties of the devices were characterized using a home-built measurement system combining a laser diode, oscilloscope (Tektronix, TDS2012B) and optical chopper, as seen in Figure 3a.

## Supporting Information

Supporting Information is available from the Wiley Online Library or from the author.

## Acknowledgements

G.T. and H.L. contributed equally to this work. This work was financed by the NSFC under No. U1632151, 61674075, 11274155, and 61204050, the Scientific and Technological Support Program in Jiangsu province under No. BE2014147-2, the Open Research Fund of State Key Laboratory of Pulsed Power Laser Technology of China (Hefei, SKL 2015 KF 04), JSNSFC No. BK20150275, Jiangsu Shuangchuang Team's and Personal Program, the Jiangsu Excellent Young Scholar Program, and the Fundamental Research Funds for the Central Universities.

## Conflict of Interest

The authors declare no conflict of interest.

## Keywords

dual-phase inorganic perovskites, flexible devices, photo responsivity, physical vapor deposition

Received: July 22, 2017
Revised: October 28, 2017
Published online: December 20, 2017

[1] Y. P. Zhang, J. Y. Liu, Z. Y. Wang, Y. Z. Xue, Q. D. Ou, L. Polavarapu, J. L. Zheng, X. Qi, Q. L. Bao, *Chem. Commun.* **2016**, *52*, 13637.
[2] G. Q. Tong, Z. H. Song, C. D. Li, Y. L. Zhao, L. W. Yu, J. Xu, Y. Jiang, Y. Sheng, Y. Shi, K. J. Chen, *RSC Adv.* **2017**, *7*, 19457.
[3] Y. Zhao, K. Zhu, *Chem. Soc. Rev.* **2016**, *45*, 655.
[4] Y. N. Chen, M. H. He, J. J. Peng, Y. Sun, Z. Q. Liang, *Adv. Sci.* **2016**, *3*, 1500392.
[5] C. T. Zuo, H. J. Bolink, H. W. Han, J. S. Huang, D. Cahen, L. Ding, *Adv. Sci.* **2016**, *3*, 1500324.
[6] Z. Zheng, F. W. Zhuge, Y. G. Wang, J. B. Zhang, L. Gan, X. Zhou, H. Q. Li, T. Y. Zhai, *Adv. Funct. Mater.* **2017**, *27*, 1703115.
[7] D. J. Yu, F. Cao, Y. L. Shen, X. H. Liu, Y. Zhu, H. B. Zeng, *J. Phys. Chem. Lett.* **2017**, *8*, 2565.
[8] National Renewable Energy Laboratory, Best Research Cell Efficiency, http://www.nrel.gov/ncpv/images/efficiency_chart.jpg (accessed: January 2016).
[9] J. Liang, C. X. Wang, Y. R. Wang, Z. R. Xu, Z. P. Lu, Y. Ma, H. F. Zhu, Y. Hu, C. C. Xiao, X. Yi, G. Y. Zhu, H. L. Lv, L. B. Ma, T. Chen, Z. X. Tie, Z. Jin, J. Liu, *J. Am. Chem. Soc.* **2016**, *138*, 15829.
[10] X. M. Li, Y. Wu, S. L. Zhang, B. Cai, Y. Gu, J. Z. Song, H. B. Zeng, *Adv. Funct. Mater.* **2016**, *26*, 2435.
[11] X. M. Li, F. Cao, D. J. Yu, J. Chen, Z. G. Sun, Y. L. Shen, Y. Zhu, L. Wang, Y. Wei, Y. Wu, H. Zeng, *Small* **2017**, *13*, 1603996.
[12] C. X. Huo, B. Cai, Z. Yuan, B. W. Ma, H. B. Zeng, *Small Methods* **2017**, *1*, 1600018.
[13] G. Q. Tong, X. Z. Lan, Z. H. Song, G. P. Li, H. Li, L. W. Yu, J. Xu, Y. Jiang, Y. Sheng, Y. Shi, K. J. Chen, *Mater. Today Energy* **2017**, *5*, 173.
[14] A. Swarnkar, A. R. Marshall, E. M. Sanehira, B. D. Chernomordik, D. T. Moore, J. A. Christians, T. Chakrabarti, J. M. Luther, *Science* **2016**, *354*, 92.
[15] J. Z. Song, L. M. Xu, J. J. Li, J. Xue, Y. H. Dong, X. M. Li, H. B. Zeng, *Adv. Mater.* **2016**, *28*, 4861.
[16] X. M. Li, D. J. Yu, J. Chen, Y. Wang, F. Cao, Y. Wei, Y. Wu, L. Wang, Y. Zhu, Z. G. Sun, J. P. Ji, Y. L. Shen, H. D. Sun, H. B. Zeng, *ACS Nano* **2017**, *11*, 2015.
[17] P. Ramasamy, D. H. Lim, B. Kim, S. H. Lee, M. S. Lee, J. S. Lee, *Chem. Commun.* **2016**, *52*, 2067.
[18] J. N. Chen, S. S. Zhou, S. Y. Jin, H. Q. Li, T. Y. Zhai, *J. Mater. Chem. C* **2016**, *4*, 11.
[19] Q. Chen, H. P. Zhou, Z. R. Hong, S. Luo, H. S. Duan, H. H. Wang, Y. S. Liu, G. Li, Y. Yang, *J. Am. Chem. Soc.* **2014**, *136*, 622.
[20] M. Z. Liu, M. B. Johnston, H. J. Snaith, *Nature* **2013**, *501*, 395.
[21] C. W. Chen, H. W. Kang, S. Y. Hsiao, P. F. Yang, K. M. Chiang, H. W. Lin, *Adv. Mater.* **2014**, *26*, 6647.
[22] G. Q. Tong, X. S. Geng, Y. Q. Yu, L. W. Yu, J. Xu, Y. Jiang, Y. Sheng, Y. Shi, K. J. Chen, *RSC Adv.* **2017**, *7*, 18224.
[23] X. Li, D. Q. Bi, C. Y. Yi, J.-D. Décoppet, J. S. Luo, S. M. Zakeeruddin, A. Hagfeldt, M. Grätzel, *Science* **2016**, *353*, 58.
[24] C. Y. Chen, H. Y. Lin, K. M. Chiang, W. L. Tsai, Y. C. Huang, C. S. Tsao, H. W. Lin, *Adv. Mater.* **2017**, *29*, 1605290.
[25] Q. S. Ma, S. J. Huang, X. M. Wen, M. A. Green, A. W. Y. Ho-Baillie, *Adv. Energy Mater.* **2016**, *6*, 1502202.
[26] X. Y. Zhang, C. Sun, Y. Zhang, H. Wu, C. Y. Ji, Y. H. Chuai, P. Wang, S. P. Wen, C. F. Zhang, W. W. Yu, *J. Phys. Chem. Lett.* **2016**, *7*, 4602.
[27] J. Xue, Y. Gu, Q. S. Shan, Y. S. Zou, J. Z. Song, L. M. Xu, Y. H. Dong, J. H. Li, H. B. Zeng, *Angew. Chem., Int. Ed.* **2017**, *56*, 5232.
[28] L. A. Frolova, D. V. Anokhin, A. A. Piryazev, S. Y. Luchkin, N. N. Dremova, K. J. Stevenson, P. A. Troshin, *J. Phys. Chem. Lett.* **2017**, *8*, 67.
[29] K. H. Wang, L. Wu, L. Li, H. B. Yao, H.S. Qian, S. H. Yu, *Angew. Chem., Int. Ed.* **2016**, *55*, 8328.
[30] G. P. Li, H. Wang, Z. F. Zhu, Y. J. Chang, T. Zhang, Z. H. Song, Y. Jiang, *Chem. Commun.* **2016**, *52*, 11296.
[31] X. L. Zhang, B. Xu, J. B. Zhang, Y. Gao, Y. J. Zheng, K. Wang, X. W. Sun, *Adv. Funct. Mater.* **2016**, *26*, 4595.
[32] H. R. Xia, J. Li, W. T. Sun, L. M. Peng, *Chem. Commun.* **2014**, *50*, 13695.
[33] J. Mao, Y. Q. Yu, L. Wang, X. J. Zhang, Y. M. Wang, Z. B. Shao, J. S. Jie, *Adv. Sci.* **2016**, *3*, 1600018.
[34] H. T. Wei, D. DeSantis, W. Wei, Y. H. Deng, D. Y. Guo, T. J. Savenije, L. Cao, J. S. Huang, *Nat. Mater.* **2017**, *16*, 826.
[35] X. H. Zhang, S. Z. Yang, H. Zhou, J. W. Liang, H. W. Liu, H. Xia, X. L. Zhu, Y. Jiang, Q. L. Zhang, W. Hu, X. J. Zhuang, H. J. Liu, W. D. Hu, X. Wang, A. L. Pan, *Adv. Mater.* **2017**, *29*, 1604431.
[36] L. Shen, Y. Z. Lin, C. X. Bao, Y. Bai, Y. H. Deng, M. M. Wang, T. Li, Y. F Lu, A. Gruverman, W. W. Li, J. S. Huang, *Mater. Horiz.* **2017**, *4*, 242.
[37] Y. J. Fang, J. S. Huang, *Adv. Mater.* **2015**, *27*, 2804.
[38] D.-H. Kwak, D.-H. Lim, H.-S. Ra, P. Ramasamy, J.-S. Lee, *RSC Adv.* **2016**, *6*, 65252.
[39] X. S. Zhang, Q. Wang, Z. W. Jin, J. R. Zhang, S. Z. Liu, *Nanoscale* **2017**, *9*, 6278.
[40] L. F. Lv, Y. B. Xu, H. H. Fang, W. J. Luo, F. J. Xu, L. M. Liu, B. W. Wang, X. F. Zhang, D. Yang, W. D. Hu, A. G. Dong, *Nanoscale* **2016**, *8*, 13589.
[41] X. S. Tang, Z. Q. Zu, H. B. Shao, W. Hu, M. Zhou, M. Deng, W. W. Chen, Z. G. Zang, T. Zhu, J. M. Xue, *Nanoscale* **2016**, *8*, 15158.
[42] S. F. Zhuo, J. F. Zhang, Y. M. Shi, Y. Huang, B. Zhang, *Angew. Chem., Int. Ed.* **2015**, *54*, 5693.
[43] X. Hu, X. D. Zhang, L. Liang, J. Bao, S. Li, W. L. Yang, Y. Xie, *Adv. Funct. Mater.* **2014**, *24*, 7373.
[44] M. Spina, M. Lehmann, B. Nafradi, L. Bernard, E. Bonvin, R. Gaal, A. Magrez, L. Forro, E. Horvath, *Small* **2015**, *11*, 4824.
[45] G. H. Chen, Y. Q. Yu, K. Zheng, T. Ding, W. L. Wang, Y. Jiang, Q. Yang, *Small* **2015**, *11*, 2848.
[46] W. Hu, R. S. Wu, S. Z. Yang, P. Fan, J. L. Yang, A. L. Pan, *J. Phys. D: Appl. Phys.* **2017**, *50*, 375101.
[47] R. Dong, Y. J. Fang, J. Chae, J. Dai, Z. G. Xiao, Q. F. Dong, Y. B. Yuan, A. Centrone, X. C. Zeng, J. S. Huang, *Adv. Mater.* **2015**, *27*, 1912.
[48] W. Hu, W. Huang, S. Z. Yang, X. Wang, Z. Y. Jiang, X. L. Zhu, H. Zhou, H. J. Liu, Q. L. Zhang, X. J. Zhuang, J. L. Yang, D. H. Kim, A. L. Pan, *Adv. Mater.* **2017**, *29*, 703256.
[49] A. Marchioro, J. Teuscher, D. Friedrich, M. Kunst, R. Van De Krol, T. Moehl, M. Grätzel, J.-E. Moser, *Nat. Photonics* **2014**, *8*, 250.
[50] Q. Chen, H. P. Zhou, T. B. Song, S. Luo, Z. R. Hong, H. S. Duan, L. T. Dou, Y. S. Liu, Y. Yang, *Nano Lett.* **2014**, *14*, 4158.